LAWRENCE
LIVERMORE
NATIONAL
LABORATORY

LLNL-JRNL-844991

Ramp compression of tantalum to multi-terapascals: Constraints of the thermal equation of state to 2.3 TPa and 5000 K

M. G. Gorman, C. J. Wu, R. F. Smith, L. X. Benedict, C. J. Prisbrey, W. Schill, S. A. Bonev, R. W. Long, P. Soderlind, D. Braun, D. C. Swift, R. Briggs, T. J. Volz, E. F. O'Bannon, P. M. Celliers, D. E. Fratanduono, J. H. Eggert, S. J. Ali, J. M. McNaney

February 9, 2023

Physical Review B

Disclaimer

Ramp compression of tantalum to multi-terapascals: Constraints of the thermal equation of state to 2.3 TPa and 5000 K

M. G. Gorman,[1,*] C. J. Wu,[1,†] R. F. Smith,[1] L. X. Benedict,[1] C. J. Prisbrey,[1] W. Schill,[1] S. A. Bonev,[1] R. W. Long,[1] P. Söderlind,[1] D. Braun,[1] D. C. Swift,[1] R. Briggs,[1] T. J. Volz,[1] E. F. O'Bannon,[1] P. M. Celliers,[1] D. E. Fratanduono,[1] J. H. Eggert,[1] S. J. Ali,[1] and J. M. McNaney[1]

[1]*Lawrence Livermore National Laboratory, 7000 East Avenue, Livermore CA 94500, USA*

(Dated: January 5, 2023)

We report measurements of the compressibility of ramp compressed tantalum to a final stress of 2.3 terapascals corresponding to 3-fold volumetric compression. Using these data, we extended the experimental constraint on the Ta cold compression curve by an order of magnitude in pressure. By combining these new data with previous measurements of shock compression, and ambient pressure heating, we construct a new, experimentally bounded and thermodynamically consistent equation of state model for Ta which has 2 % uncertainty in pressure at 1 TPa. We therefore propose Ta as a new *in situ* pressure scale for laser-heated static compression experiments which have recently been able to reach terapascal pressures and thousands of degrees Kelvin. Our new EOS of Ta is experimentally constrained at extreme pressures and temperatures relevant to a wide range of planetary interiors and will allow for more accurate comparison between experimental measurements and theory at extreme conditions.

INTRODUCTION

Extreme pressures and temperatures can dramatically change the structure, bonding, and mechanical properties of materials. Indeed, coupling the laser-heated diamond anvil cell (LHDAC) with in situ x-ray diffraction techniques led to numerous important discoveries ranging from novel material syntheses [1, 2] to understanding material properties at planetary interiors conditions above 100 GPa [3]. The recent coupling of laser heating techniques with double staged (ds-DAC) and toroidal (t-DAC) diamond anvil cells [4], where the sample is compressed statically between two opposing diamonds with culet sizes of ~ 20 μm, now facilitates the study of novel material behavior above 1 TPa (1 TPa = 10 million atmospheres) and several thousand Kelvin. However, a key challenge of such experiments is accurately determining the sample pressure at elevated temperatures due to the lack of an experimentally benchmarked high-temperature pressure standard. In addition, noble metals have often been chosen as pressure standards for room temperature static compression studies due to their high x-ray scattering efficiency, simple crystal structure and phase stability up to extreme pressures. However, some have recently been shown to undergo structural phase transformations at high temperature [5–9] and so may not be suitable as standards at elevated temperatures. This means that new candidate materials may be necessary for thermal pressure standards at terapascal conditions.

Shock compression experiments, where the sample is compressed discontinuously can be used to provide absolute measurements of stress and density along a path known as the Hugoniot (purple curve in Figure 1). However, such compression also generates significant heating which means that the study of solid matter is precluded for most materials above 0.2-0.3 TPa. Conversely, laser-driven ramp compression provides an avenue for high pressure - low temperature studies, meaning that sample materials can remain in the solid phase at extreme pressures and densities. The sample follows a compression path close to the principal isentrope (blue curve in Figure 1). This technique was used recently to establish high accuracy pressure benchmarks for Cu, Au and Pt to beyond 1 TPa at room temperature [10, 11]. However, such measurements do little to bound the thermal components of the equation of state (EOS), meaning that considerable uncertainty still exists in the pressure (P) - density (ρ) relation as a function of temperature (T). By combining experimental measurements which sample different thermodynamic compression paths, the opportunity exists to develop an experimentally bounded EOS which is valid to extreme densities and high temperatures relevant for double staged DAC experiments.

Tantalum is a material that exhibits remarkable phase stability up to extreme pressures and temperatures [18, 19], has a body-centered cubic (bcc) crystal structure, and high x-ray scattering efficiency. In this work, we present ramp compression measurements of Ta up to 2.3 TPa and 53.0 g/cm^3 representing three-fold volumetric compression. These new measurements extend the experimental constraints on the Ta cold curve by an order of magnitude in pressure, which, taken together with previous experimental measurements under shock compression [19–25], and isobaric heating [26], allow for the construction of an experimentally benchmarked high-temperature EOS of Ta at terapascal pressures. This new model which has uncertainties of 2 % at pressures of 1 TPa, will serve as an accurate high-temperature pressure standard for use in static-compression experiments.

EOS models consist of cold (T-independent) contributions, and thermal pieces (accounting for ionic and elec-

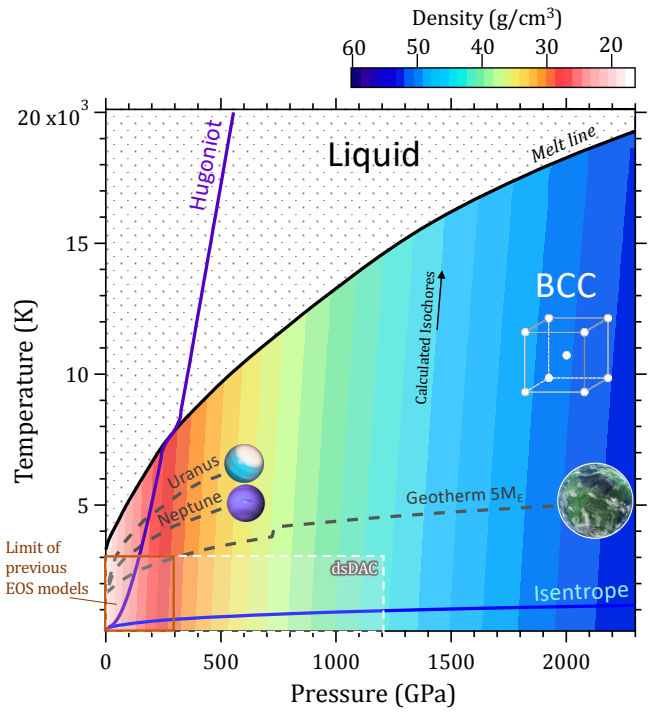

FIG. 1. The temperature-pressure phase diagram of Ta. Recent advances in static compression have enabled the study of matter beyond 1 TPa at elevated temperatures (white dashed box). Laser driven ramp compression allows materials to be studied in their solid form to extreme pressures close to an isentrope (blue line). Shock compression achieves states along a thermodynamic path called the Hugoniot (purple line). New ramp compression measurements presented here, in addition with previous experimental data sets allow for the construction of an accurate high temperature Ta EOS far beyond the conditions constrained previously [12–15] (orange box). Temperature-pressure conditions similar to those found in planetary interiors are now within the operating limits of our new EOS (grey dashed lines) [16, 17] . The melt curve, density color map and isochores are outputs of our new high-temperature EOS.

tronic excitations). Prior to the advent of high-pressure ramp compression data, EOS models were constrained by fitting the cold contribution to DAC data, the low-pressure part of the thermal terms to thermal expansion (obtained from both ambient heating and high-pressure high-temperature DAC experiments) and specific heat measurements, and the high-pressure thermal terms to shock Hugoniot data. However, there is a problem with this strategy: It is generally not the case that DAC and shock data exist over the *same* range of ρ for any material. Thus, when a wide-ranged EOS model is desired, one is forced to extrapolate the DAC-derived $P_{cold}(\rho)$ to values of ρ beyond the static high-P data itself, so that the difference with the shock data can be used to extract the thermal component. This leads to uncertainties in EOS which grow with both P and T, as discussed in Ref. [27]. The addition of ramp-compression overcomes this difficulty by augmenting the DAC-derived $P_{cold}(\rho)$ at low-ρ with additional $P(\rho)$ data at higher-ρ, into (and even well beyond) the compression regime of single and double-shock data. These data lie close to an isentrope, and are therefore at significantly lower-T than that of the shock Hugoniot, as illustrated for Ta in Fig. 1. An added benefit is that this locus of states sample solid-state compression, and are closer in T to the interior conditions of planets, leading to an EOS model which is better constrained for these astrophysical applications.

In this work, we use new Ta ramp-compression measurements, together with existing isobaric and shock-wave data to make an accurate EOS model for Ta without appealing to high-ρ extrapolations of $P_{cold}(\rho)$. In so doing, we provide the high-pressure science community with a more accurate standard for the determination of pressure at large compressions and temperatures.

RAMP COMPRESSION OF TANTALUM USING LASERS

To directly constrain the cold curve up to multi-TPa pressures, we ramp compressed Ta using the National Ignition Facility (NIF). The experimental and analysis techniques used in this work have been described elsewhere [10, 11, 28] and are summarized here (for more information, see Appendices A-C). We used up to 1.5 MJ of laser energy in 168 beams of NIF in a 30 ns pulse to ramp compress Ta samples up to a peak pressure of 2.30 TPa. Laser intensity was incident on a gold hohlraum, generating an x-ray bath which directly ablated the target package mounted on an opening at its side (Fig. 2a). The target package consists of a Cu ablator and a four-step Ta brick (Fig. 2a). The ablation drive imparted an initial low pressure (76-117 GPa) steady shock on the Ta sample, followed by a monotonically increasing ramp-pressure wave. The gradual nature of the compression ensures the Ta sample follows a much cooler thermodynamic path relative to the Hugoniot and thus remains in the solid phase up to extreme pressures (see Fig. 1) [10]. The Ta sample consisted of four steps of thicknesses approximately 91 / 96 / 101 / 106 μm (Fig. 2a) and width of 200 μm. A velocity interferometer system for any reflector (VISAR) [29] was used to measure the free surface velocity history $U_{FS}(t)$ for each thickness (Fig. 2a) during compression. The multistep nature of the target is key, as the difference in wave arrival times at two different sample depths allows for the absolute determination of the Lagrangian sound speed as a function of particle velocity ($C_L(u_p)$) [30]. By integrating $C_L(u_p)$, we can extract the longitudinal stress-density relation and the associated uncertainties along a ramp compression path. Crucially, unlike EOS experiments performed in a DAC, the data here do not rely on a standard to determine the

stress-density relationship.

The region of $C_L(u_p)$ below the initial shock state is obtained using an EOS model for Ta [31] which is assumed to correctly describe the isentropic release down to zero pressure. C_L and its uncertainty $\sigma_{C_L}(u_p)$ were obtained from thickness and velocity-versus-time data by linear regression using errors determined by our measurement accuracies. Figure 2b shows the Lagrangian sound speed versus particle velocity for seven NIF experiments on Ta along with 1-σ uncertainties and the weighted average of these experiments. Our data is in excellent agreement with previous laser driven ramp compression experiments on Ta [32]. $C_L(u_p)$ and $\sigma_{C_L}(u_p)$ are integrated to obtain

$$P_x = P_H + \rho_0[\int_{u_{p,H}}^{u_p} C_L \ , du_p] \tag{1}$$

and

$$\rho = ([1/\rho_H] - [1/\rho_0] \times [\int_{u_{p,H}}^{u_p} du_p/C_L])^{-1} \tag{2}$$

and their uncertainties

$$\sigma_{P_x}^2 = \sigma_{P_{x,H}}^2 + \rho_0[\int_{u_{p,H}}^{u_p} \sigma_{C_L}\, du_p] \tag{3}$$

and

$$\sigma_\rho^2 = ([\rho_H^2/\rho_0^2])\delta\rho_H)^2 + ([\rho^2/\rho_0] \times [\int_{u_{p,H}}^{u_p} [\sigma_{C_L}/C_L^2] du_p])^2 \tag{4}$$

Here, P_H, ρ_H, and $u_{p,H}$ are the pressure, density, and particle velocity, respectively, associated with the initial shock Hugoniot state. Uncertainties are propagated through the integrals linearly, rather than in quadrature because they appear to be strongly correlated rather than random. This method of uncertainty propagation allows for the direct propagation of experimental uncertainties.

We make several corrections to reduce the measured longitudinal stress (σ_x) to the isentropic pressure (P_{isen}). First, the thermal pressure associated with the initial shock state is accounted for, reducing the stress-density along the shock-ramp path to a shockless stress-density path. The temperature at the initial shock state is estimated from using a previous tabular EOS of Ta [33], and the thermal pressure difference is approximated as : $P_{shock-ramp} - \mathrm{P}_{shockless} = \gamma\rho(E_{th}(T_{shock-ramp}) - E_{th}(T_s)$, where E_{th} is the thermal energy at density ρ and temperature $T_{shock-ramp}$ along the shock-ramp path or temperature T_s along the shockless compression path as determined from the Debye integral and γ is the Gruneisen parameter. The temperature along the shock-ramp path is determined from integrating the thermodynamic derivative $\gamma\frac{s}{\rho}$ [34]. To relate the measured longitudinal stress to an equivalent hydrostatic pressure we assume the Von Mises criterion: $\sigma_x = P_{hyd} + 2/3Y(P)$

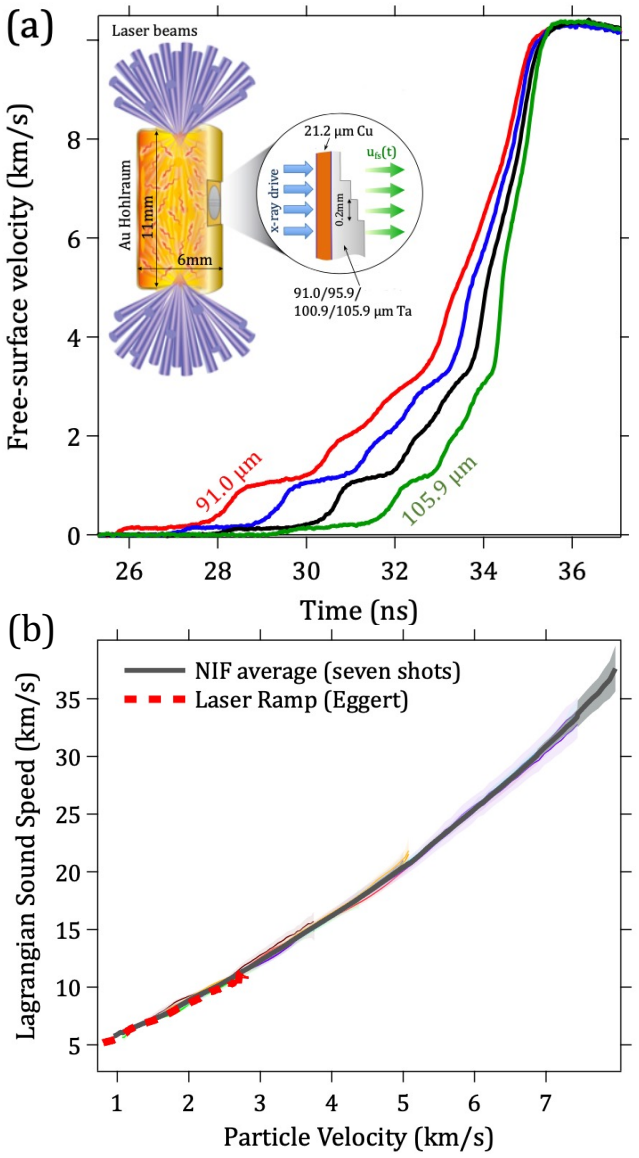

FIG. 2. (a) A temporally-shaped laser pulse irradiates an Au hohlraum which generates an x-ray bath and launches a gradual compression wave into the stepped Ta sample. A spatially resolving VISAR records the free surface velocity history from each of the 4 steps (colored traces). (b) Ta Lagrangian sound speed versus particle velocity for seven NIF experiments on Ta are shown with 1-σ uncertainties. The averaged stress-density response is shown in black. Data from previous laser experiments are shown for comparison [32].

where Y is the yield strength. If a solid supports strength at high pressure, the thermal pressure from plastic work heating must also be accounted for. Plastic work heating causes the pressure on the hydrostat to deviate from the isentrope by P_{hyd} - $\mathrm{P}_{isen} = \gamma\rho\int_0^{\epsilon_x} \beta\, dW_P$, where ϵ_x is the natural strain $\log(\rho/\rho_0)$, β is the Taylor-Quinney factor, which describes the fraction of plastic work that

partitions into the thermal energy of the system. Here, β is assumed to be = 1, which assumes all plastic work is used to heat the material [35]. dW_p is the plastic work heating. To make these corrections and reduce our measurements of longitudinal stress to isentropic pressure, we require a model for the Grüneisen parameter (γ(P)), the plastic work heating (dW_P) and the yield strength (Y_P) (See Supplementary materials Section C). Figure 3 shows the percentage correction as a function of stress for the deviatoric stress, plastic work heating and initial shock heating terms. The magnitude of the total correction when reducing our ramp path to the principle isentrope is $\sim$ 4% at 2.3 TPa (black curve in Fig. 3). To determine the pressure along the 298 K isotherm or cold curve, one must subtract the thermal pressure from the isentrope at the elevated temperature along the isentrope, T_s. For example the pressure along the 298 K isotherm, P_{298K} = P_s - $\gamma\rho[E_{th}.(T_s)$ - $E_{th}.(298)]$ where E_{th}. is the thermal energy at density ρ determined from the Debye integral. The thermal pressure difference between the isentrope and 298 K isotherm is calculated to be very small ($\sim$5 GPa) at 2 TPa.

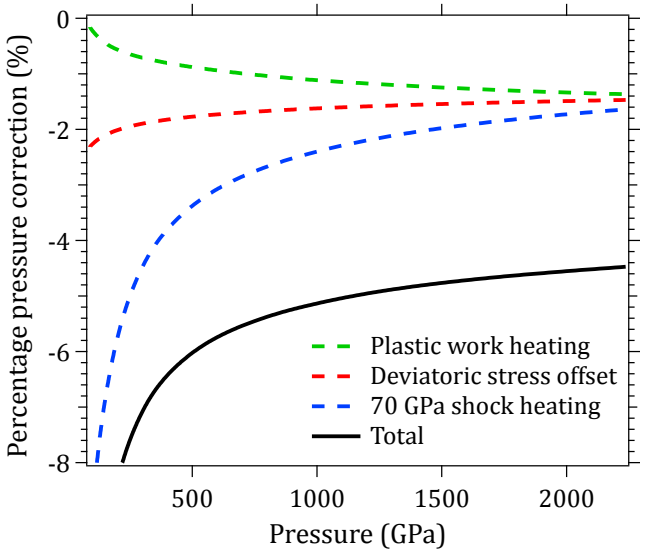

FIG. 3. The percent correction applied to reduce the measured stress-density response to a hydrostatic pressure-density isentrope. The total correction is $\sim$4% at 2.3 TPa

Figure 4 shows the determined stress-density relationship of Ta up to 2.3 TPa which was averaged from 7 NIF experiments (black dash) (See Fig. S2 for data from individual experiments) and the resulting 298 K isotherm (black curve). The experimental uncertainties from stress and density are combined into a standard uncertainty in stress calculated from

$$\delta\sigma_x(\rho) = \sqrt{\delta\sigma_x(u_p)^2 + (\frac{\partial\sigma_x}{\partial\rho}\delta\rho(u_p))^2}. \quad (5)$$

It is likely that combining the uncertainties in this manner represents an overestimate of the total uncertainty as equation 5 assumes that the uncertainties in stress and density are uncorrelated. The 1-σ uncertainty in pressure of our Ta isotherm at 1 TPa is 2 %, demonstrating unprecedented precision at pressure conditions around 3 times the Earth's core. Our data are both in agreement with previous shockless compression experiments performed using laser [32] (red) and pulsed power [36, 37] (purple) and previous isotherms determined from static compression experiments (colored symbols). A comparison with previous room temperature Ta isotherms from DAC, reduced shock wave, and ultrasonic data is shown in the Fig. 4 inset. Our 298 K isotherm shows excellent agreement with isotherms from hydrostatic DAC experiments [38–40] up to pressures where they are constrained by data. Cynn and Yoo [38] used a Au pressure standard in their study and used an Au EOS from Heinz and Jeanloz [41] to determine the Ta sample pressure. Interestingly, the Ta pressures determined using the Heinz and Jeanloz EOS are systematically lower than the isotherm determined from this work (see Fig. S7). However, by reinterpreting the Cynn and Yoo data using an updated Au pressure standard recently established from ramp compression [11], we find the agreement between the Ta compression data of Cynn and Yoo and this work improves considerably (maroon curve in Fig. 4 inset). The isotherm of Ref [42], which was determined from data which extended up to 0.31 TPa, is stiffer than our 298 K isotherm, most likely due to the non hydrostatic conditions in which the Ta samples where compressed in those experiments as no pressure transmitting medium was used. Our 298 K isotherm is key to the construction of an accurate high-T EOS of Ta as it bounds the $P_{cold}(\rho)$ up to 2.3 TPa which is the dominant contribution to the total material response at TPa pressures and temperatures of several thousand Kelvin.

CONSTRAINING THE NEW TANTALUM EQUATION OF STATE MODEL

We now describe the construction of a new Ta EOS model which uses our ramp compression measurements as a primary constraint. As described above, this fixes $P_{cold}(\rho)$ up to 2.3 TPa. To further constrain the EOS of Ta at elevated temperature, we utilize a wealth of existing experimental data. The key constraints for the thermal component of the EOS include: (1) thermodynamic data (T-dependent density, entropy, and enthalpy) near ambient pressure; (2) melt temperatures, $T_{melt}(P)$, at both ambient and elevated pressures as measured in laser-heated DACs below 100 GPa and informed by the shock melting study of Kraus et al. at several hundred GPa [19]; (3) DFT-based molecular dynamics predictions of isochores of internal energy, pressure, and en-

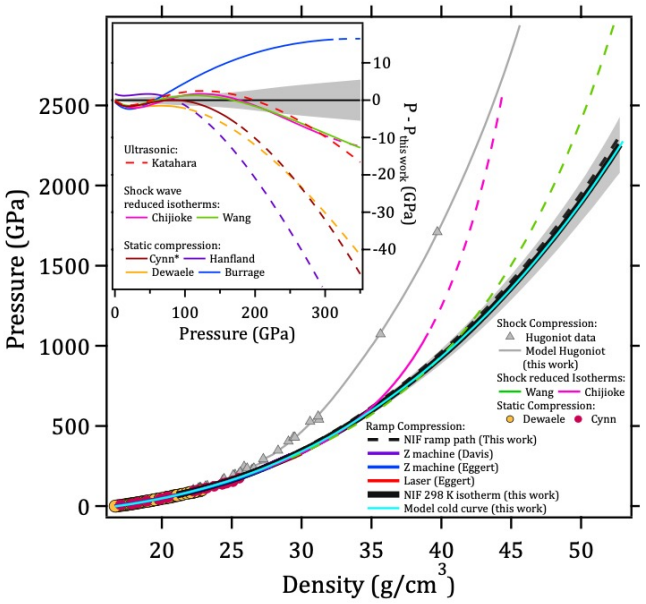

FIG. 4. The pressure-density response of Ta to pressures up to 2.3 TPa and 53 g/cm^3. The measured stress (black dash) and 298 K isotherm (black) are shown. The error bars represent 1σ standard deviation of multiple measurements collected and averaged into a single result, which also includes measurement uncertainties. Previous ramp compression data from pulsed power [36, 37] (blue and purple) and laser [32] (red) experiments, shock wave reduced isotherms [43, 44] (pink and green) are shown as colored lines. Shock-wave [20–25] (grey symbols) and static data [38, 40] (red and orange symbols) are shown for comparison. The computed cold curve and Hugoniot of the new EOS are shown by cyan and grey curves respectively. Inset - Comparison of room temperature isotherms from previous studies [38–40, 42–45] and the 298 K isotherm determined in this work. Solid lines denote the regions where the isotherms are constrained by data and dashed lines indicate extrapolations. The asterisk indicates that the data of Cynn has been reinterpreted using a new EOS of Au [11] (see main text.)

tropy, which were used to supplement experimental constraints in regions inaccessible by experiment, and (4) shock Hugoniot data [20–25] used to constrain thermal pressure $P_{thermal}(\rho, E)$ as a function of density and internal energy (See 5 and Figs. S9-13). These experimental shock data extend up to pressures of ∼2.5 TPa and were collected using two-stage gas guns and convergent explosive drives. Regarding $T_{melt}(P)$, it is noteworthy that when fitting to the DAC melting data of Dewaele et al. [40], we made use of their measured T_{melt} vs. ρ relationship; $T_{melt}(P)$ was then determined from our EOS model (see Fig. S12).

Importantly, recent measurements of the shock melting pressure [19] provide an additional connection between this E-dependent function and the temperature. We use previous isobaric heating data to constrain the specific heat (C_V) [26] and previous ambient pressure melting data to constrain the entropy of melting [46] (Fig. S9). We employ various models to capture the complete EOS behavior of Ta which will be discussed in more detail below. The parameters of each model are varied in concert until a satisfactory agreement with all experimental data is obtained. We utilized the multiphase equation of state generation code [47], developed at Lawrence Livermore National Laboratory to aid in this iterative fitting process.

Model forms

The models we use for the cold and thermal terms of the free energy are the same as those employed in Ref. [47]. We take the Helmholtz free energy, $F = E - TS$ (where S is the entropy), for each phase (solid, liquid) to be decomposed into a cold (T-independent) piece, an ionic excitation term, and an electronic excitation term,

$$F(\rho, T) = E_{\rm cold}(\rho) + F_{\rm ion}(\rho, T) + F_{\rm electron}(\rho, T). \quad (6)$$

For the cold term, we use a Vinet-Rose analytic form in the neighborhood of ambient density [48], which is then joined through spline interpolation to a higher-density form derived from the results of DFT calculations. Note that we use the construct of a cold piece even for the liquid, though this phase is not thermodynamically favored at low T. For the ionic excitation term, we employ a Debye model, with phase-dependent and density-dependent Debye temperature, $\theta(\rho)$,

$$F_{\rm Debye}(\rho, T) =$$

$$k_{\rm B}T\left[\frac{9}{8}\frac{\theta(\rho)}{T} + 3\ln\left[1 - \exp[-\theta(\rho)/T]\right] + D[\theta(\rho)/T]\right], \quad (7)$$

where

$$D[y] = \frac{3}{y^3}\int_0^y \frac{x^3}{e^x - 1}. \quad (8)$$

Since the first term, equal to $9/8k_{\rm B}\cdot\theta$ and arising from quantum zero-point motion, is independent of T, we subsume it into $E_{\rm cold}(\rho)$ and assign the remainder to the ionic excitation term,

$$F_{\rm ion}(\rho, T) = F_{\rm Debye}(\rho, T) - \frac{9}{8}k_{\rm B}\theta(\rho). \quad (9)$$

We take the electronic excitation component from a DFT spherical atom-in-jellium model known as PURGATORIO [49], which is an update of the earlier INFERNO [50] model. This neglects the directionality of chemical bonding, but includes electronic ionization (due to both temperature and pressure) in detail. As in Ref.[47], we

use this contribution for *both* solid and liquid phases of Ta, where the $T = 0$ PURGATORIO bonding contribution is subtracted off to yield the contribution to electronic excitations, specifically,

$$F_{\rm electron}(\rho,T) =$$

$$F_{\rm PURGATORIO}(\rho,T) - F_{\rm PURGATORIO}(\rho,T=0). \quad (10)$$

We also add our Cell Model contribution [51] to the ion-thermal term for the liquid phase; this ensures that $\lim_{T\longrightarrow\infty} E_{\rm ion}(\rho,T) = \frac{3}{2}k_{\rm B}T$ per ion, and $\lim_{T\longrightarrow\infty} P_{\rm ion}(\rho,T) = k_{\rm B}T\rho/m_{\rm ion}$, as required for the ideal gas EOS to be reached (though we mention this addition for completeness, it is of negligible import for the fitting to the DAC, shock, and ramp compression data of primary concern in this work).

Model fitting and validation

Given that our choice of $F_{\rm electron}$ is fixed by simulations, our fitting of the new EOS model for Ta involves the specification of four ρ-dependent functions: $E_{\rm cold}^{\rm solid}(\rho)$, $\theta^{\rm solid}(\rho)$, $E_{\rm cold}^{\rm liquid}(\rho)$, and $\theta^{\rm liquid}(\rho)$, where $E_{\rm cold}^{\rm liquid}(\rho) - E_{\rm cold}^{\rm solid}(\rho)$ is the major contributor to the solid-liquid internal energy difference, and $\theta^{\rm solid}(\rho)/\theta^{\rm liquid}(\rho)$ is the major contributor to the entropy difference. Our strategy is to use DAC isotherm measurements and this work's ramp compression data (see the solid black curve of Fig. 4) to constrain $P_{\rm cold}^{\rm solid}(\rho)$ ($= \frac{\rho^2}{m_{\rm Ta}}\frac{dE_{\rm cold}^{\rm solid}}{d\rho}$, shown as the cyan curve in Fig. 4), and experimental measurements of the following quantities to constrain the functions $E_{\rm cold}^{\rm liquid}(\rho)$, $\theta^{solid}(\rho)$, and $\theta^{\rm liquid}(\rho)$: 1) ambient pressure thermal expansion, 2) ambient pressure entropy, 3) $T_{\rm melt}(\rho)$, 4) shock Hugoniot $P(\rho)$, and 5) pressures of intersection between the Hugoniot and the melt curve. In addition to these constraining data, we augment them with DFT-MD inferences of the solid entropy along two isochores (ρ= 16.7025 g/cm^3, and 30.5927 g/cm^3). The fitting procedure we use is an iterative one, where $E_{\rm cold}^{\rm solid}(\rho)$, $\theta^{\rm solid}(\rho)$, $E_{\rm cold}^{\rm liquid}(\rho)$, and $\theta^{\rm liquid}(\rho)$ are varied in concert until a satisfactory agreement with all data is obtained. This is aided by our use of the MEOS multiphase equation of state generation code [47].

In practice, the $\theta(\rho)$ functions are determined by first constraining them at low-ρ from the ambient-pressure entropy (inferred from specific heat data), and then their elevated-ρ behavior is extracted by inverting the relationship:

$$\gamma_{\rm ion}(\rho) = \frac{\rho}{\theta(\rho)}\cdot\frac{d\theta}{d\rho} \quad , \quad (11)$$

where $\gamma_{\rm ion}$ is the ionic Grüneisen parameter, which itself is extracted from the high-T ($T > \theta$) behavior of the ionic pressure,

$$P_{\rm ion}(\rho, T > \theta) = \frac{C_{\rm V}T}{V}\gamma_{\rm ion}(\rho), \quad (12)$$

where V ($= m_{\rm Ta}/\rho$) is the atomic volume and C_V is the constant-volume specific heat. Our values for $P_{\rm ion}$ are culled from the total thermal contribution, after subtracting the electronic contribution to the pressure resulting from Eq.10. The total thermal contribution (ionic + electronic) to the pressure is obtained from $P_{\rm total} - P_{\rm cold}$; indeed, it is here that the inclusion of our ramp compression data is crucial, as it provides a tight constraint on $P_{\rm cold}(\rho)$ throughout the full range of ρ where $P_{\rm total}^{\rm Hugoniot}(\rho)$ is obtainable from shock data.

Figure 5a shows our fit to the ambient pressure thermal expansion data of Touloukian et al. for the solid phase [52]. Figure 5b displays agreement between our new Ta EOS and DFT-MD calculations of the total entropy of solid Ta along the isochore ρ= 30.5927 g/cm^3. Here, the DFT-MD entropy predictions were made by us using a procedure akin to that presented in the work of Teweldeberhan et al. [54]. This agreement ensures that our choice of $\theta^{\rm solid}(\rho)$ at these densities is reasonable. We deem this to be particularly important, since entropy at elevated pressures is a quantity which is still unconstrained by direct experimental measurement. We also ensured agreement with our lower-ρ DFT-MD entropy isochore at 16.7025 g/cm^3. Figure 5c shows a large collection of $P(\rho)$ principal shock Hugoniot data, along with the principal Hugoniot of our EOS model (also shown in Fig. 4 by grey triangles and grey curve). Agreement with these data was affected by choosing $\gamma_{\rm ion}(\rho)$ (see Eqs.9, 11 and 12), once $E_{\rm cold}(\rho)$ had been constrained by a combination of DAC isotherm data and the NIF ramp compression measurements presented above. Figure 5d presents comparisons between our EOS model and experimental data of pressure vs. particle velocity for (assumed adiabatic) releases from various shock states. Here, the solid black line is the principal Hugoniot of our EOS model, and the colored dashed lines represent our model's isentropes launched from various Hugoniot states. Note the excellent agreement throughout, suggesting that our high-T, low-ρ liquid free energy model is accurate in this regime. This lends further credence to our choice of $\gamma_{\rm ion}^{\rm liquid}(\rho)$ at low-ρ.

Figure 6 shows an illustration of tantalum's T vs. P phase diagram once again, but now with the locations of the various experimental and *ab initio* theoretical constraints superposed. We note here that unlike for the other constraints, the principal Hugoniot constraint (red curve) is really a constraint in P vs. ρ; the temperature (y-axis) of this red curve in Fig. 6 is a *prediction* of our EOS model. Nevertheless, our match to the pressures of intersection between the Hugoniot and T_{melt} (shown as the red vertical lines) are key to our determination of the latent heat of melting (involving both the solid-liquid

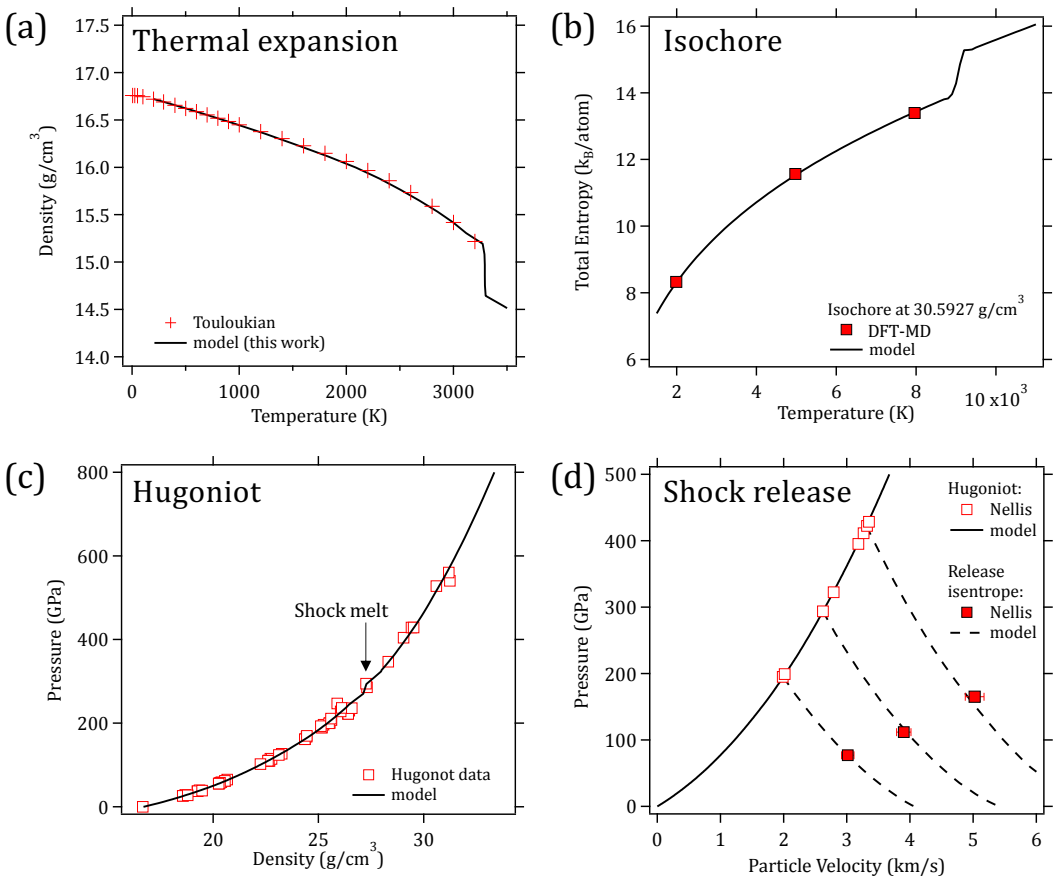

FIG. 5. Comparison of high-temperature experimental and theory data on Ta with our new EOS model. a) Ambient pressure heating data from Touloukian et al. [52] b) A 30.5927 g/cm^3 isochore determine from DFT based molecular dynamics simulations. c) Shock Hugoniot data obtained by two-stage gas gun and convergent explosive drive experiments. [20–25] d) Shock release data from two-stage gas gun experiments [53]. The parameters of our high-temperature EOS model are varied until excellent agreement is found with these data (see main text).

internal energy difference, and the entropy difference) assumed within our Ta EOS model.

DISCUSSION

There have been several previous attempts to construct a high-T EOS of Ta using classical molecular dynamics [56] first principles molecular dynamics [12–14] and also semi-empirically [15], as in this work. However, these previous studies are all limited in pressure up to between 0.1- 0.3 TPa as they relied on previous DAC data to anchor the $P_{cold}(\rho)$. Along a 3000 K isotherm, the pressure disagreement between previous models is already as high as ∼10% at 0.25 TPa (Fig. S8), and continues to diverge at higher pressures. Our new EOS is experimentally constrained and accurate up to pressures temperatures far beyond the stated applicability limits of these previous models (Fig. 1 and Fig. S8), due to its enforced agreement with the ramp compression measurements up to 2.3 TPa.

This significant advancement in high-T EOS development, brought about by laser-driven ramp compression, coincides with a recent experimental breakthrough in static compression, where laser heating techniques were successfully coupled with a ds-DAC, allowing sample conditions beyond 1 TPa and ∼3000 K to be accessed [4]. In such experiments, x-ray diffraction is used to determine the sample density under compression, while pyrometric techniques are used to estimate sample temperature [57]. The ability to access such extreme conditions is promising for novel material syntheses as the first results from such experiments have demonstrated the recovery of new rhenium alloys [4]. In planetary science, the potential surface habitability of newly-discovered rocky exoplanets is dependent on planetary interior conditions which, for example on Earth, result in tectonic activity, surface outgassing, and the production of a magnetosphere. These extreme interior states of matter can now be investigated through high-pressure, high-temperature ex-

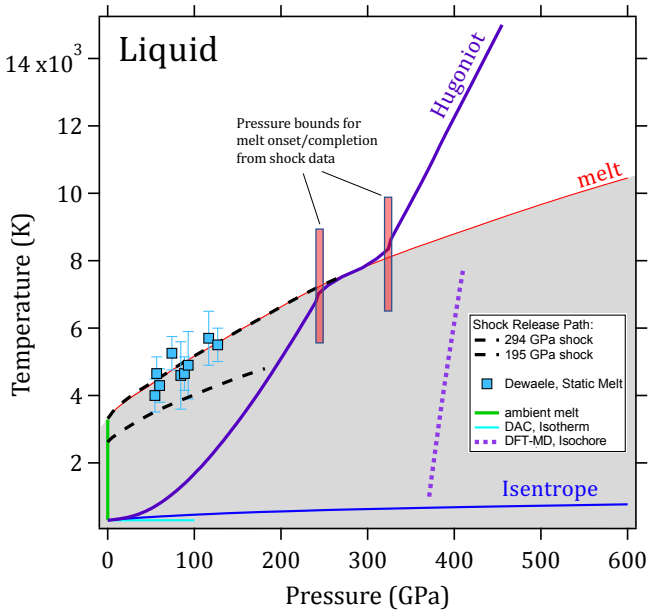

FIG. 6. Temperature - pressure phase diagram of Ta which shows the experimental constraints used in the construction of the high-T EOS. Ramp compression (blue) and 300 K DAC [40] (cyan) data provide constraints on $P_{cold}(\rho)$. Existing ambient pressure heating [52] (green), laser heated DAC [55] (cyan markers), Hugoniot (purple), and shock melting [19] (red bars) data are used to constrain $P_{thermal}(\rho, T)$. Comparison with isochores calculated at high pressure using DFT-based molecular dynamics (purple dotted) and release isentropes measured from plate impact experiments [53] (black dashed) provide scrutiny of the performance of the EOS.

periments where the composition and crystal structure of core-mantle constituents are predicted to transform above $\sim$ 1 TPa and 4000 K for a 10 Earth mass rocky exoplanet [58] (Fig. 1).

Our new wider-ranged Ta EOS model renders this material the only one with a P-ρ-T EOS which is well constrained at the conditions relevant to these new physics frontiers which are now accessible by coupling laser heating to ds-DAC compression. By its inclusion in the sample chamber, Ta could be used as a high-temperature pressure standard where the Ta pressure state, assumed to be in equilibrium with the sample of interest, can be determined directly from the diffraction data at a known temperature. Chemical reaction between the sample, standard and diamonds [55] can be minimized with the use of single pulse laser heating set ups [59] that have sub-millisecond heating pulse durations.

Accordingly, we have fitted several isotherms from our model to a Vinet EOS and have provided the fitting parameters for the 298 K, 1000 K, 2000 K, 3000 K, 4000 K and 5000 K isotherms in Table I. The form of the Vinet fitting follows Refs [10, 43, 44, 60] and is $P(X) = 3K_0[(1-X^{1/3})/X^{2/3}]\exp[\eta(1-X^{1/3}) + \beta(1-X^{1/3})^2 + \Psi(1-X^{1/3})^3]$ where $X = \rho/\rho_0, K_0$ is the bulk moduls and η,β and Ψ are other fitting parameters. We recommend using our isotherms up to 2.3 TPa and 5000 K.

TABLE I. Best-fit parameters for a third-order Vinet fit to the calculated isotherms at 298 K, 1000 K, 2000 K, 3000 K, 4000 K and 5000 K from our high-T EOS of tantalum. The initial densities for each isotherm were taken to be 16.650 g/cm^3, 16.444 g/cm^3, 16.038 g/cm^3, 15.415 g/cm^3, 14.778 g/cm^3 and 13.503 g/cm^3 respectively.

T (K)	K_0 (GPa)	η	β	Ψ
298	179.60(2.18)	4.68(0.16)	-0.22(0.72)	10.08(1.03)
1000	175.9(2.21)	4.46(0.17)	0.72(0.73)	8.79(1.04)
2000	161.88(2.06)	4.42(0.17)	1.24(0.72)	7.76(1.00)
3000	128.67(1.81)	5.46(0.18)	-2.20(0.73)	11.75(0.98)
4000	104.00(1.71)	6.13(0.20)	-4.00(0.79)	13.41(1.02)
5000	51.86(1.26)	9.69(0.27)	-14.30(1.00)	23.66(1.20)

CONCLUSION

In conclusion, we have measured the isentropic compression of tantalum to 2.3 TPa. From this, we have constructed an experimentally constrained high-T EOS for tantalum up to multi-TPa pressures and many thousands of degrees Kelvin, which will serve as a means to determine pressure at extreme compressions and elevated temperatures now achievable using laser heated ds-DACs. While Ta may be a promising high-T pressure standard, our work represents a general method for high-T EOS construction. Ramp compression experiments have also been performed on other materials to multi-terapascal pressures [10, 11, 28] providing a road map for building an accurate high-T EOS catalogue at extreme conditions.

ACKNOWLEDGEMENTS

We thank the laser and target fabrication staff of the NIF. This work was performed under the auspices of the U.S. Department of Energy by Lawrence Livermore National Laboratory under Contract No. DE-AC52-07NA27344.

* Correspondence to gorman11@llnl.gov
† Correspondence to wu5@llnl.gov

[1] A. Friedrich, B. Winkler, L. Bayarjargal, W. Morgenroth, E. A. Juarez-Arellano, V. Milman, K. Refson, M. Kunz, and K. Chen, Phys. Rev. Lett. **105**, 085504 (2010).
[2] E. Gregoryanz, C. Sanloup, M. Somayazulu, J. Badro, G. Fiquet, H.-k. Mao, and R. J. Hemley, Nat. Mater. **3**, 294 (2004).

[3] S. Anzellini, A. Dewaele, M. Mezouar, P. Loubeyre, and G. Morard, Science **340**, 464 (2013).

[4] L. Dubrovinsky, S. Khandarkhaeva, T. Fedotenko, D. Laniel, M. Bykov, C. Giacobbe, E. Lawrence Bright, P. Sedmak, S. Chariton, V. Prakapenka, A. V. Ponomareva, E. A. Smirnova, M. P. Belov, F. Tasndi, N. Shulumba, F. Trybel, I. A. Abrikosov, and N. Dubrovinskaia, Nature **605**, 274 (2022).

[5] R. Briggs, F. Coppari, M. G. Gorman, R. F. Smith, S. J. Tracy, A. L. Coleman, A. Fernandez-Pañella, M. Millot, J. H. Eggert, and D. E. Fratanduono, Phys. Rev. Lett. **123**, 045701 (2019).

[6] S. M. Sharma, S. J. Turneaure, J. M. Winey, and Y. M. Gupta, Phys. Rev. B **102**, 020103 (2020).

[7] S. M. Sharma, S. J. Turneaure, J. M. Winey, and Y. M. Gupta, Phys. Rev. Lett. **124**, 235701 (2020).

[8] S. K. Han, R. F. Smith, D. Kim, J. K. Wicks, J. R. Rygg, A. Lazicki, J. H. Eggert, and T. S. Duffy, Phys. Rev. B **103**, 184109 (2021).

[9] M. Sims, R. Briggs, T. J. Volz, S. Singh, S. Hamel, A. L. Coleman, F. Coppari, D. J. Erskine, M. G. Gorman, B. Sadigh, J. Belof, J. H. Eggert, R. F. Smith, and J. K. Wicks, J. Appl. Phys. **132**, 075902 (2022).

[10] D. E. Fratanduono, R. F. Smith, S. J. Ali, D. G. Braun, A. Fernandez-Pañella, S. Zhang, R. G. Kraus, F. Coppari, J. M. McNaney, M. C. Marshall, L. E. Kirch, D. C. Swift, M. Millot, J. K. Wicks, and J. H. Eggert, Phys. Rev. Lett. **124**, 015701 (2020).

[11] D. E. Fratanduono, M. Millot, D. G. Braun, S. J. Ali, A. Fernandez-Pañella, C. T. Seagle, J.-P. Davis, J. L. Brown, Y. Akahama, R. G. Kraus, M. C. Marshall, R. F. Smith, E. F. O'Bannon, J. M. McNaney, and J. H. Eggert, Science **372**, 1063 (2021).

[12] S. Ono, Int. J. Mol. Sci. **10**, 4342 (2009).

[13] R. E. Cohen and O. Gülseren, Phys. Rev. B **63**, 224101 (2001).

[14] S. Taioli, C. Cazorla, M. J. Gillan, and D. Alfè, J. Phys.: Conf. Series **121**, 012010 (2008).

[15] P. I. Dorogokupets and A. R. Oganov, Phys. Rev. B **75**, 024115 (2007).

[16] R. F. Smith, D. E. Fratanduono, D. G. Braun, T. S. Duffy, J. K. Wicks, P. M. Celliers, S. J. Ali, A. Fernandez-Pañella, R. G. Kraus, D. C. Swift, *et al.*, Nature Astronomy **2**, 452 (2018).

[17] N. Nettelmann, R. Helled, J. Fortney, and R. Redmer, Planetary and Space Science **77**, 143 (2013).

[18] D. Orlikowski, P. Söderlind, and J. A. Moriarty, Phys. Rev. B **74**, 054109 (2006).

[19] R. G. Kraus, F. Coppari, D. E. Fratanduono, R. F. Smith, A. Lazicki, C. Wehrenberg, J. H. Eggert, J. R. Rygg, and G. W. Collins, Phys. Rev. Lett. **126**, 255701 (2021).

[20] L. V. Al'tshuler, A. A. Bakanova, I. P. Dudoladov, E. A. Dynin, R. F. Trunin, and B. S. Chekin, J. Appl. Mech. Tech. Phys. **22**, 145 (1981).

[21] R. G. McQueen, S. P. Marsh, J. W. Taylor, J. N. Fritz, and W. J. Carter, *High-Velocity Impact Phenomena*, edited by R. Kinslow (Elsevier Inc., 1970) Chap. XII.

[22] S. P. Marsh, *LASL shock Hugoniot data*, edited by S. P. Marsh (University of California Press Berkeley [etc.] ; London, 1980) p. 136.

[23] A. C. Mitchell and W. J. Nellis, J. Appl. Phys. **52**, 3363 (1981).

[24] N. C. Holmes, J. A. Moriarty, G. R. Gathers, and W. J. Nellis, J. Appl. Phys. **66**, 2962 (1989).

[25] R. F. Trunin, N. V. Panov, and A. B. Medvedev, Pis'ma v Zhurnal Ehksperimental'noj i Teoreticheskoj Fiziki **62(7-8)**, 572 (1995).

[26] G. R. Gathers, Int. J. Thermophys. **4**, 149 (1983).

[27] M. Matsui, J. Phy.: Conf. Series **215**, 012197 (2010).

[28] R. F. Smith, D. E. Fratanduono, D. G. Braun, T. S. Duffy, J. K. Wicks, P. M. Celliers, S. J. Ali, A. P. Fernandez, R. G. Kraus, D. C. Swift, G. W. Collins, and J. H. Eggert, Nat. Astron. **2**, 452 (2018).

[29] P. M. Celliers, D. K. Bradley, G. W. Collins, D. G. Hicks, T. R. Boehly, and W. J. Armstrong, Rev. Sci. Instrum. **75**, 4916 (2004).

[30] D. C. Swift, D. E. Fratanduono, R. G. Kraus, and E. A. Dowling, Rev. Sci. Instrum. **90**, 093903 (2019).

[31] C. Greeff and J. Johnson, *New Sesame equation of state for tantalum* (Los Alamos National Lab., 2000).

[32] J. Eggert, R. Smith, D. Swift, R. Rudd, D. Fratanduono, D. Braun, J. Hawreliak, J. McNaney, and G. Collins, High Pressure Research **35**, 339 (2015), https://doi.org/10.1080/08957959.2015.1071361.

[33] C. W. Greeff and J. D. Johnson, *New Sesame equation of state for tantalum*, Tech. Rep. LA-13681-MS (Los Alamos National Lab., 2000).

[34] C. Kittel and H. Kroemer, *Thermal physics*, Vol. 9690 (Wiley New York, 1970).

[35] D. Rittel, A. Bhattacharyya, B. Poon, J. Zhao, and G. Ravichandran, Materials Science and Engineering: A **447**, 65 (2007).

[36] J.-P. Davis, J. L. Brown, M. D. Knudson, and R. W. Lemke, J. Appl. Phys. **116**, 204903 (2014).

[37] J. L. Brown, J.-P. Davis, and C. T. Seagle, J. Dyn. Behav. Mater. **7**, 196 (2021).

[38] H. Cynn and C.-S. Yoo, Phys. Rev. B **59**, 8526 (1999).

[39] M. Hanfland, K. Syassen, and J. Köhler, J. Appl. Phys. **91**, 4143 (2002).

[40] A. Dewaele, P. Loubeyre, and M. Mezouar, Phys. Rev. B **69**, 092106 (2004).

[41] D. L. Heinz and R. Jeanloz, J. Appl. Phys. **55**, 885 (1984).

[42] K. C. Burrage, C. S. Perreault, E. K. Moss, J. S. Pigott, B. T. Sturtevant, J. S. Smith, N. Velisavljevic, and Y. K. Vohra, High Pressure Res. **39**, 489 (2019).

[43] Y. Wang, R. Ahuja, and B. Johansson, J. Appl. Phys. **92**, 6616 (2002).

[44] A. D. Chijioke, W. J. Nellis, and I. F. Silvera, J. Appl. Phys. **98**, 073526 (2005).

[45] K. W. Katahara, M. H. Manghnani, and E. S. Fisher, J. Appl. Phys. **47**, 434 (1976).

[46] E. S. Domalski and E. D. Hearing, *NIST Chemistry WebBook*, edited by P. J. Linstrom and W. G. Mallard (NIST Standard Reference Database Number 69; National Institute of Standards and Technology: Gaithersburg, MD., 2018) Chap. Condensed Phase Heat Capacity data, https://webbook.nist.gov/chemistry.

[47] C. J. Wu, P. C. Myint, J. E. Pask, C. J. Prisbrey, A. A. Correa, P. Suryanarayana, and J. B. Varley, J. Phys. Chem. A **125**, 1610 (2021).

[48] P. Vinet, J. Ferrante, J. H. Rose, and J. R. Smith, Journal of Geophysical Research: Solid Earth **92**, 9319 (1987), https://agupubs.onlinelibrary.wiley.com/doi/pdf/10.1029/JB092iB09

[49] B. Wilson, V. Sonnad, P. Sterne, and W. Isaacs, Journal of Quantitative Spectroscopy and Radiative Transfer **99**,

658 (2006), radiative Properties of Hot Dense Matter.
[50] D. A. Liberman, Phys. Rev. B **20**, 4981 (1979).
[51] L. X. Benedict, K. P. Driver, S. Hamel, B. Militzer, T. Qi, A. A. Correa, A. Saul, and E. Schwegler, Phys. Rev. B **89**, 224109 (2014).
[52] Y. S. Touloukian, R. Powell, C. Ho, and M. Nicolaou, *Thermophysical properties of matter-The TPRC data series. Volume 10. Thermal Diffusivity* (1974).
[53] W. Nellis, A. Mitchell, and D. Young, Journal of Applied Physics **93**, 304 (2003).
[54] A. M. Teweldeberhan, J. L. Dubois, and S. A. Bonev, Phys. Rev. Lett. **105**, 235503 (2010).
[55] A. Dewaele, M. Mezouar, N. Guignot, and P. Loubeyre, Phys. Rev. Lett. **104**, 255701 (2010).
[56] Z.-L. Liu, X.-L. Zhang, L.-C. Cai, X.-R. Chen, Q. Wu, and F.-Q. Jing, J. Phys. Chem. Solids **69**, 2833 (2008).
[57] S. Anzellini and S. Boccato, Crystals **10** (2020).
[58] T. S. Duffy and R. F. Smith, Frontiers in Earth Science **7**, 23 (2019).
[59] Z. Konôpková, W. Morgenroth, R. Husband, N. Giordano, A. Pakhomova, O. Gutowski, M. Wendt, K. Glazyrin, A. Ehnes, J. T. Delitz, A. F. Goncharov, V. B. Prakapenka, and H.-P. Liermann, Journal of Synchrotron Radiation **28**, 1747 (2021).
[60] R. G. Kraus, J.-P. Davis, C. T. Seagle, D. E. Fratanduono, D. C. Swift, J. L. Brown, and J. H. Eggert, Phys. Rev. B **93**, 134105 (2016).

A: TARGET DETAILS

The Ta samples were obtained from an annealed plate provided by H.C. Starck Inc., Newton, MA, as part of a common lot to Sandia (SNL), Los Alamos (LANL), and Lawrence Livermore National Laboratories (LLNL). Each Ta step was diamond turned to typical surface flatnesses of $\sim$ 10 nm over a 1 mm region as determined by double sided interferometry. Electron back scatter diffraction measurements of the Ta starting material indicate an average grain size of 71.7 $\pm$ 31 μm and an average aspect ratio (minor axis / major axis) of 0.51 $\pm$ 0.11 (Fig. 1). An Inverse pole figure of a typical Ta sample. Shots occurred in the z-direction (Fig. 1). Measuring 4 steps in our experiments enable redundancy which allow us to study the effect of strain rate and grain size. As the breakout in each step is uniform across the 4 steps in each experiment, we see no evidence of grain orientation effects affecting the material response.

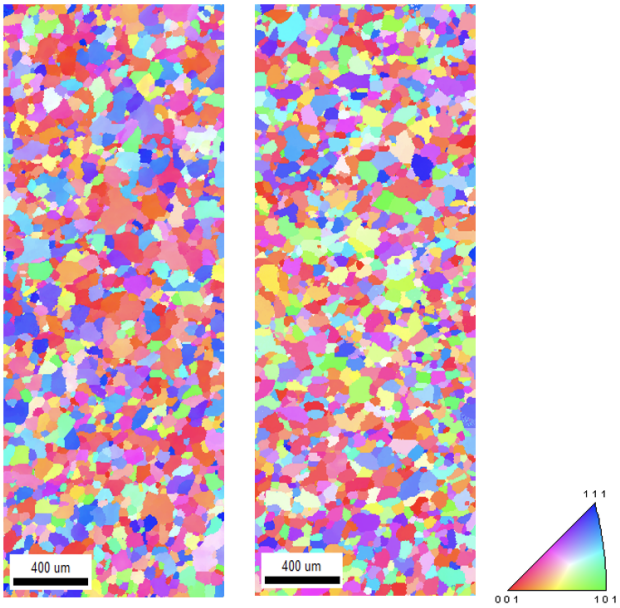

FIG. 1. Electron backscatter diffraction (EBSD) inverse pole figure maps of the initial grain structure and texture of the Ta material used in the experiments.

B: STRESS DENSITY OF INDIVIDUAL EXPERIMENTS

The stress versus density for seven NIF experiments on Ta are shown in Fig. 2 with 1-σ uncertainties. The stress ? density data are obtained from the continuous free-surface velocity measurements of the stepped Ta target. The resolution of the stress and density is ultimately dependent on the temporal and velocity resolution of the VISAR diagnostic. The temporal resolution of the VISAR is related to the properties of the streak camera and is taken to be 1-2 pixels in duration which is equal to $\sim$30 ps. The velocity resolution is dependent on the size of etalon used in the VISAR and is taken to be generally equal to $\sim$0.02 of 1 fringe which in this case is equal to $\sim$20 m/s. These experimental uncertainties, as well as the uncertainties in the target step height ($\sim$20 nm), are propagated to give typical stress uncertainties of 2% and density uncertainties of $\sim$3%. The magnitude of these uncertainties are similar to those of other ramp experiments performed at the NIF [1, 2].

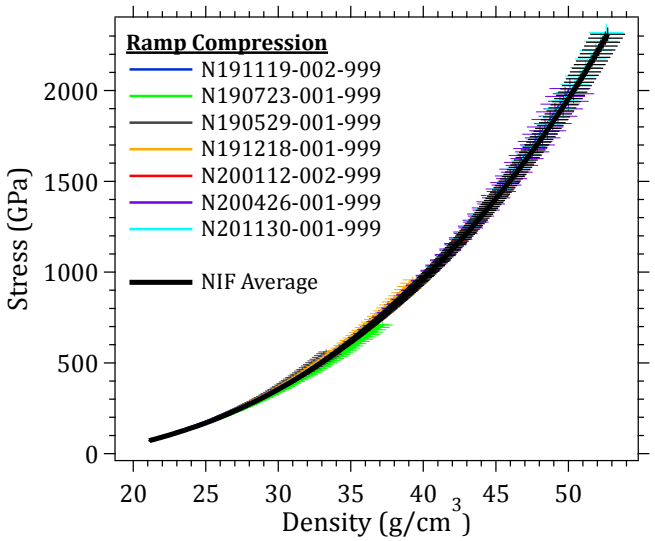

FIG. 2. Ta stress-density measurements. The stress versus density for seven NIF experiments on Ta are shown with 1-σ uncertainties. The averaged stress-density response is shown in black.

C: REDUCTION MODEL ASSUMPTIONS

For our model of density dependence of the Grüneisen parameter of solid Ta, we used several experimental constraints, including the ambient pressure thermal expansion, the solid Hugoniot below 2.3 Mbar (black markers in Fig. 3, the DFT-MD isochore near 4 Mbar and the inferno-derived gamma values obtained for extreme compressions above 70 g/cm^3. We assumed a 25% uncertainty for this model.

Following the analysis of Fowles et al. [9], plastic work heating is defined as $dW_P = (1/\rho_0)\frac{2}{3}Y[d\epsilon_x - dY/2G(\rho)]$, where G($\rho$) is the shear modulus. The high pressure strength of Ta has been estimated under shockless compression up to 0.4 TPa in pulsed power experiments [10, 11]. These data have been fit to a simple Steinberg-Cochrane-Guinan strength model (SCG) [11] which we utilize here to describe the high pressure yield strength

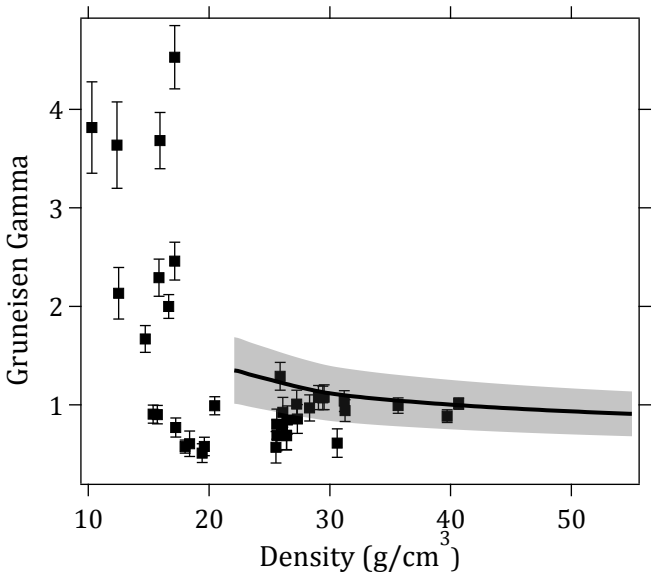

FIG. 3. Previous measurements of Grüneisen Gamma for full density and porous Ta samples under shock compression [3–8] (symbols). Given the spread in the experimental data, a 25% uncertainty is assumed for this model.

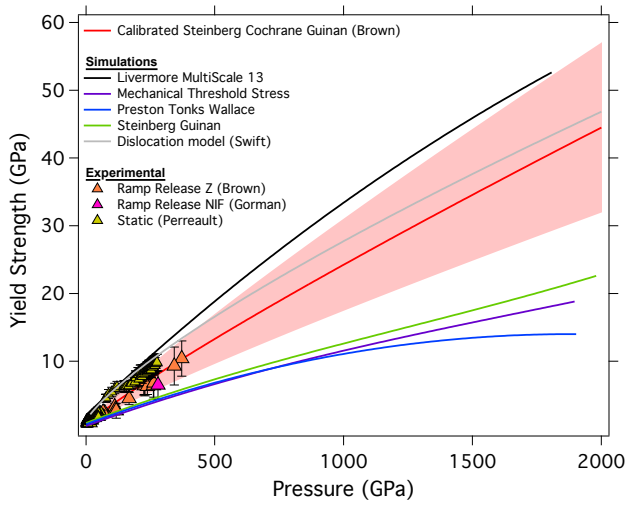

FIG. 4. Yield strength versus pressure for Ta as determined from static [15] (yellow markers), pulsed power ramp [11] (orange markers) and laser ramp (pink marker) compression experiments. Also shown are simulated yield strength vs pressure relationships using various models of Ta (colored curves). The red line is the calibrated Steinberg Cochrane Guinan model from [11] and associate 1-σ uncertainties which we use in our reduction process from ramp data to the isentrope.

behavior of Ta Fig. 4. While there has been considerable study in the compression rate effects of strength in Ta [12, 13] we believe it adequate to use a rate independent strength model here, as the material response determined in our experiments agrees within experimental uncertainty with previous pulsed power experiments [10, 11] despite a ∼20x difference in compression rate (Fig. 2b). Furthermore a laser driven ramp release experiment returned an estimate of yield strength which was very similar to the experiments performed at the Z machine (pink marker in Fig. 4). The material response of other simple metals with no low temperature phase transformations such as Cu [1, 14] Pt, and Au [2, 11] have also been studied at both NIF and the Z machine with no observable difference in behavior. The strength of Ta has been measured using x-ray diffraction techniques in a toroidal DAC up to 0.276 TPa [15] and agrees well with the Y(P) as estimated from pulsed power experiments [11] further indicating that strain rate effects are not significant to the strength of Ta at these conditions. However, for completeness, the magnitude of the strength correction, assuming a range of strength models - namely the Preston Tonks Wallace (PTW) [12] model, Livermore Multiscale (LMS) [13] model, the Mechanical threshold constitutive strength (MTS) [16] model, and a new dislocation based model [17] - was calculated (Fig. 4)

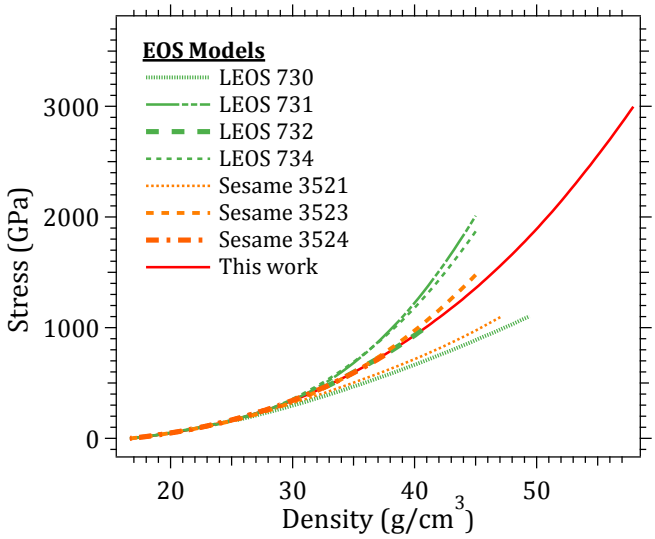

FIG. 5. Comparison of the 298 K isotherm as determined from the ramp compression experiments from this work with previous tabular EOS models of Ta.

D: TABULAR EXPERIMENTAL DATA

The uncorrected stress-density relationship as determined from our ramp compression experiments, and the corresponding isentrope and 298 K isotherm obtained after performing corrections (see Details on Reduction Process section) are provided in table I.

E: FORM OF THE EQUATION OF STATE FITTING FUNCTION

Several functional forms where fitted to the 298 K isotherm determined from our new EOS model including the Vinet-Rose [18] and third-order Birch Murnaghan [19]. However, both these functional forms did not fit the 298 K isotherm satisfactorily (Fig. 6). It was found that a third-order Vinet functional form [20] accurately fit the data over the entire density range.

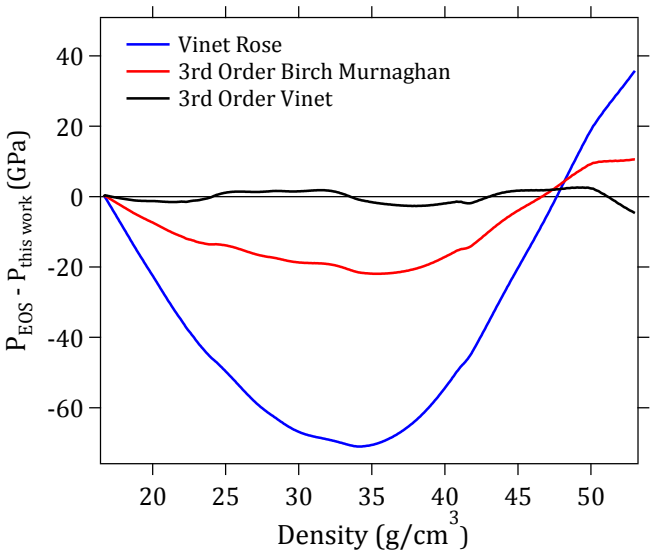

FIG. 6. Difference plot showing how well various EOS functional forms fit the 298 K isotherm of our new Ta EOS. As can be seen, the third order Vinet functional form provides a far superior fit to the isotherm relative to the Vinet-rose or third order Birch Murnaghan formulations.

F: ADDITIONAL EOS MODEL FITTING AND VALIDATION

Figure 9 shows our fits to the ambient pressure thermal expansion data for the solid and liquid phase, and our fit to the T-dependent entropy data of both solid and liquid (panel b). We choose to prioritize the 2 kbar liquid expansion data of Berthault over the 1 kbar data of Gathers (see panel a), as we find it to be more consistent with other data used in our fitting.

Figure 10 shows the comparisons between our EOS model and experimental data of pressure vs. particle velocity for (assumed adiabatic) releases from various shock states. Here, the solid black line is the principal Hugoniot of our EOS model, and the colored dashed lines represent our model's isentropes launched from various Hugoniot states. Note the excellent agreement throughout, suggesting that our high-T, low-ρ liquid free energy model is accurate in this regime. This lends further credence to

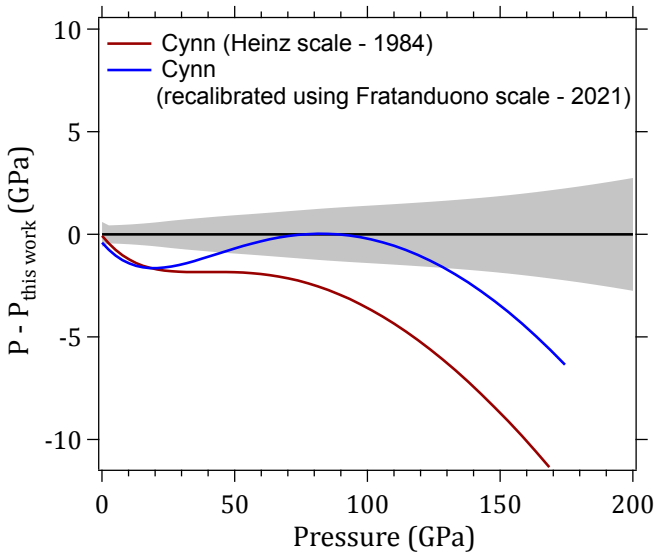

FIG. 7. Difference plot which shows a comparison of the 298 K isotherm from Cynn [21] with the 298 K isotherm from this work. After reinterpreting the data of Cynn using a more accurate pressure scale of Fratanduono [2] the agreement with this work improved considerably.

our choice of $\gamma_{\rm ion}^{\rm liquid}(\rho)$ at low-ρ, as these particular data were not used in our fitting procedure.

For the density-functional-theory (DFT) calculations we rely on an all-electron full-potential linear muffin-tin orbitals (FPLMTO) method [29]. It is characterized by its atomic-like basis functions and for Ta we include 5s, 5p, 4d, and 4f semi-core and 6s, 6p, 5d, and 5f as valence states that are allowed to hybridize in one energy window. The total number of valence electrons for Ta is thus 37 in these calculations. We employ the local-density approximation (LDA) and the generalized gradient approximation (GGA). Spin-orbit coupling is included for the d and f states as described in [30]. Figure 11 displays our NIF ramp compression data (including error bars) once again, along with the principal isentrope of L736 (solid black line), and the results of two different DFT calculations of the solid Ta cold pressure (dashed lines). The fact that our model is in agreement with the ramp data is by construction, since we used these data as a primary constraint for $P_{\rm cold}^{\rm solid}(\rho)$. However, the observation that the two DFT predictions (each employing a different exchange-correlation functional) are well within the experimental error bars is significant, as this is the first such experimental test of DFT at such high compressions for a high-Z metal such as Ta.

Figure 12 shows our fit to the DAC melt data of Dewaele et al. [32], which covers a range of pressures between 0.5 Mbar and 1.3 Mbar (our agreement with the ambient $T_{\rm melt}$ is exhibited above in Fig. 9, as well as in the lower-left of Fig. 12). We took care to fit specifi-

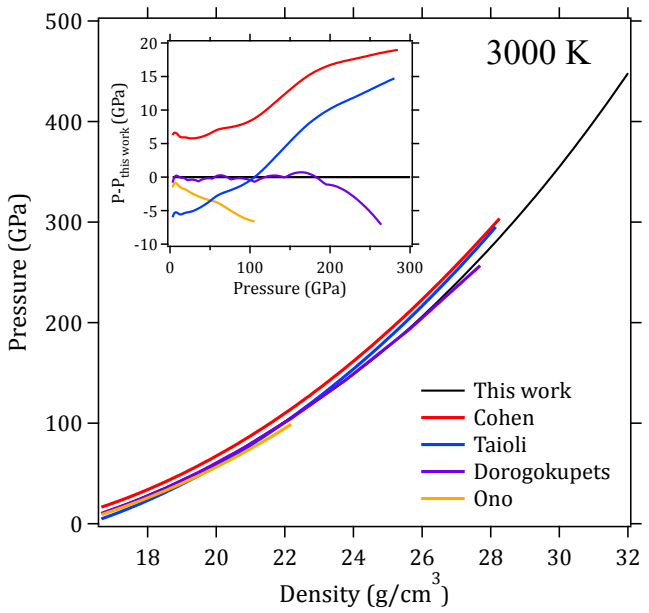

FIG. 8. Pressure-density relations for Ta along a 3000 K isotherm from previous high-temperature equations of states of Ta [22–25] (colored lines). The 3000 K from this work is shown by the black curve. Inset - Pressure difference plot of the previous high-T EOSs and this work.

cally to the experimental $T_{\rm melt}(\rho)$ data, rather than to the $T_{\rm melt}(P)$ as also reported in Dewaele et al., because these authors used the EOS model of Dorogokupets et al. [25] (indicated in Fig. 12 as the DO EOS) to relate their measured $T_{\rm melt}(\rho)$ to a $T_{\rm melt}(P)$; since L736 is notably different from the DO EOS, our interpretation of the DAC melt data in pressure (red symbols) is slightly different from that from the DO EOS (blue symbols) presented in Dewaele et al. [32].

Figure 13 displays agreement between L736 and DFT-MD calculations of the total entropy of liquid Ta along a ρ= 16.7025 g/cm^3 isochore.

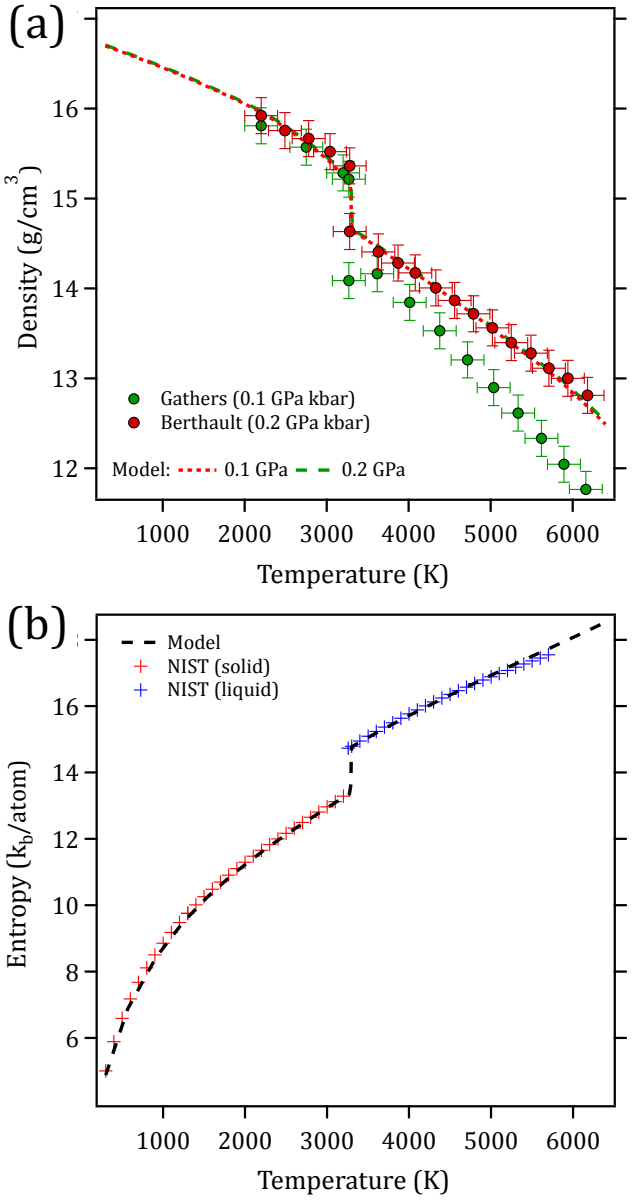

FIG. 9. a) Comparison of ambient pressure thermal expansion data for the solid and liquid phase and our EOS model [26, 27]. b) Comparison of the T-dependent entropy data of both solid and liquid [28] and our EOS model (panel b).

[1] D. E. Fratanduono, R. F. Smith, S. J. Ali, D. G. Braun, A. Fernandez-Pañella, S. Zhang, R. G. Kraus, F. Coppari, J. M. McNaney, M. C. Marshall, L. E. Kirch, D. C. Swift, M. Millot, J. K. Wicks, and J. H. Eggert, Phys. Rev. Lett. **124**, 015701 (2020).

[2] D. E. Fratanduono, M. Millot, D. G. Braun, S. J. Ali, A. Fernandez-Pañella, C. T. Seagle, J.-P. Davis, J. L. Brown, Y. Akahama, R. G. Kraus, M. C. Marshall, R. F. Smith, E. F. O'Bannon, J. M. McNaney, and J. H. Eggert, Science **372**, 1063 (2021).

[3] L. V. Al'tshuler, A. A. Bakanova, I. P. Dudoladov, E. A. Dynin, R. F. Trunin, and B. S. Chekin, J. Appl. Mech. Tech. Phys. **22**, 145 (1981).

[4] R. G. McQueen, S. P. Marsh, J. W. Taylor, J. N. Fritz, and W. J. Carter, *High-Velocity Impact Phenomena*, edited by R. Kinslow (Elsevier Inc., 1970) Chap. XII.

[5] S. P. Marsh, *LASL shock Hugoniot data*, edited by S. P. Marsh (University of California Press Berkeley [etc.] ; London, 1980) p. 136.

[6] A. C. Mitchell and W. J. Nellis, J. Appl. Phys. **52**, 3363 (1981).

[7] N. C. Holmes, J. A. Moriarty, G. R. Gathers, and W. J. Nellis, J. Appl. Phys. **66**, 2962 (1989).

[8] R. F. Trunin, N. V. Panov, and A. B. Medvedev, Pis'ma v Zhurnal Ehksperimental'noj i Teoreticheskoj Fiziki **62(7-8)**, 572 (1995).

[9] R. Fowles and R. F. Williams, J. Appl. Phys. **41**, 360

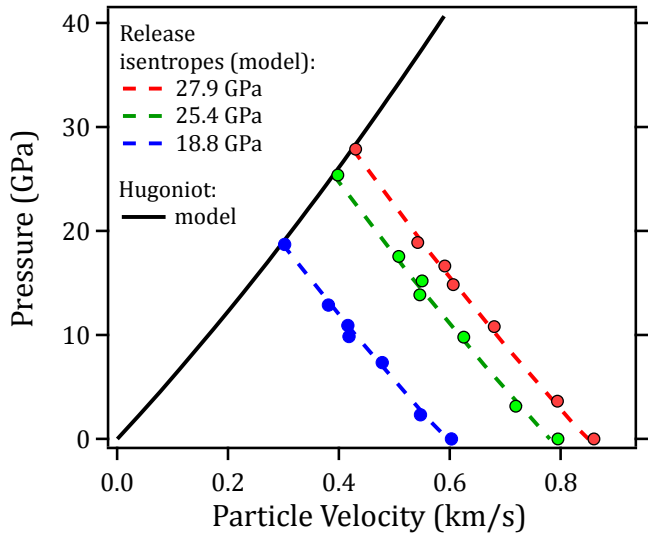

FIG. 10. Comparisons between our EOS model and experimental data of pressure vs. particle velocity for (assumed adiabatic) releases from various shock states.

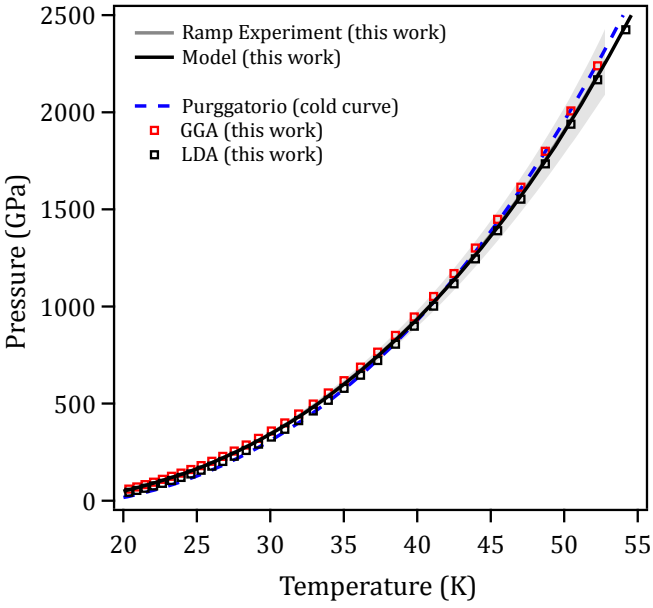

FIG. 11. Comparison of the isentrope determined from our NIF ramp compression experiments with the isentrope from our new EOS model and also two different DFT calculations of solid Ta.

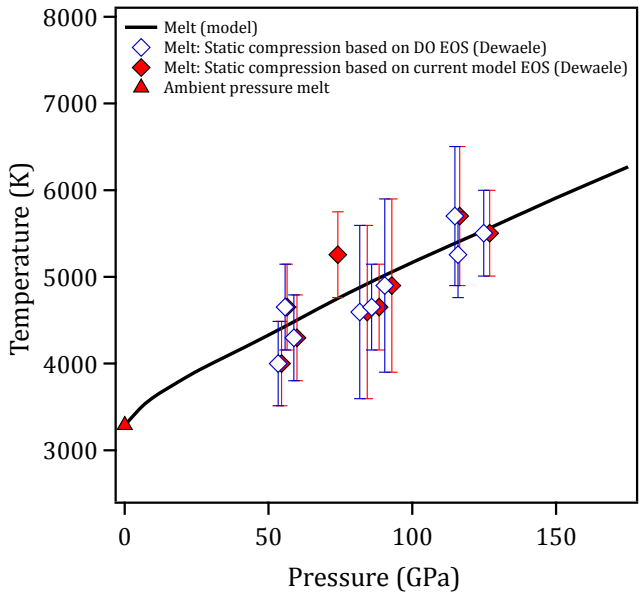

FIG. 12. Our EOS Fit to the DAC melt data of Dewaele et al. [31], which covers a range of pressures between 0.5 Mbar and 1.3 Mbar. The pressure states have been reinterpreted from the original work (See main text).

(1970).
[10] J.-P. Davis, J. L. Brown, M. D. Knudson, and R. W. Lemke, J. Appl. Phys. **116**, 204903 (2014).
[11] J. L. Brown, J.-P. Davis, and C. T. Seagle, J. Dyn. Behav. Mater. **7**, 196 (2021).
[12] D. L. Preston, D. L. Tonks, and D. C. Wallace, Journal of Applied Physics **93**, 211 (2003).
[13] N. R. Barton and M. Rhee, J. Appl. Phys. **114**, 123507 (2013).
[14] R. G. Kraus, J.-P. Davis, C. T. Seagle, D. E. Fratanduono, D. C. Swift, J. L. Brown, and J. H. Eggert, Phys. Rev. B **93**, 134105 (2016).
[15] C. Perreault, L. Q. Huston, K. Burrage, S. C. Couper, L. Miyagi, E. K. Moss, J. S. Pigott, J. S. Smith, N. Velisavljevic, Y. Vohra, and B. T. Sturtevant, J. Appl. Phys. **131**, 015905 (2022).
[16] P. S. Follansbee and U. F. Kocks, Acta Metall. **36**, 81 (1988).
[17] D. C. Swift, K. Alidoost, R. Austin, T. Lockard, C. Wu, S. Hamel, J. E. Klepeis, and P. Peralta, arXiv preprint arXiv:2110.06345 (2021).
[18] P. Vinet, J. Ferrante, J. H. Rose, and J. R. Smith, Journal of Geophysical Research: Solid Earth **92**, 9319 (1987), https://agupubs.onlinelibrary.wiley.com/doi/pdf/10.1029/JB092iB09
[19] F. Birch, Journal of Applied Physics **9**, 279 (1938), https://doi.org/10.1063/1.1710417.
[20] P. Vinet, J. H. Rose, J. Ferrante, and J. R. Smith, Journal of Physics: Condensed Matter **1**, 1941 (1989).
[21] H. Cynn and C.-S. Yoo, Phys. Rev. B **59**, 8526 (1999).
[22] S. Ono, Int. J. Mol. Sci. **10**, 4342 (2009).
[23] R. E. Cohen and O. Gülseren, Phys. Rev. B **63**, 224101 (2001).
[24] S. Taioli, C. Cazorla, M. J. Gillan, and D. Alfè, J. Phys.: Conf. Series **121**, 012010 (2008).
[25] P. I. Dorogokupets and A. R. Oganov, Phys. Rev. B **75**, 024115 (2007).
[26] G. R. Gathers, Int. J. Thermophys. **4**, 149 (1983).
[27] A. Berthault, L. Arles, and J. Matricon, International journal of thermophysics **7**, 167 (1986).
[28] E. S. Domalski and E. D. Hearing, *NIST Chemistry WebBook*, edited by P. J. Linstrom and W. G. Mallard

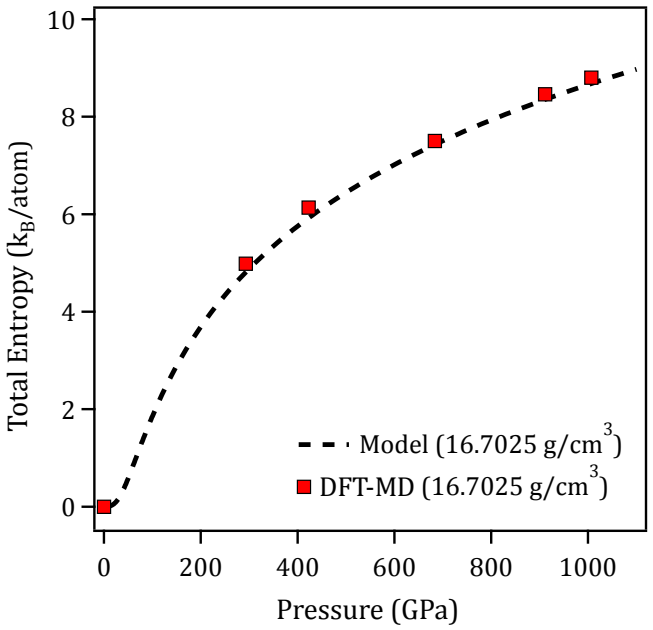

FIG. 13. DFT-MD calculations of the total entropy of liquid Ta along a ρ= 16.7025 g/cm^3 isochore and the fit from our new EOS model.

(NIST Standard Reference Database Number 69; National Institute of Standards and Technology: Gaithersburg, MD., 2018) Chap. Condensed Phase Heat Capacity data, https://webbook.nist.gov/chemistry.

[29] J. M. Wills, M. Alouani, P. Andersson, A. Delin, O. Eriksson, and O. Grechnyev, *Full-Potential Electronic Structure Method: energy and force calculations with density functional and dynamical mean field theory*, Vol. 167 (Springer Science & Business Media, 2010).

[30] L. Nordström, J. Wills, P. H. Andersson, P. Söderlind, and O. Eriksson, Physical Review B **63**, 035103 (2000).

[31] A. Dewaele, M. Mezouar, N. Guignot, and P. Loubeyre, Phys. Rev. Lett. **104**, 255701 (2010).

[32] A. Dewaele, P. Loubeyre, and M. Mezouar, Phys. Rev. B **69**, 092106 (2004).

Ramp Path		Isentrope		298 K Isotherm		
Stress (GPa)	**σ Stress (GPa)**	**Pressure (GPa)**	**σ Pressure (GPa)**	**Pressure (GPa)**	**σ Pressure (GPa)**	**ρ (g/cm^3)**
72.10	1.91	70.38	0.00	70.38	0.00	21.10
77.52	0.11	75.68	0.46	75.52	0.46	21.36
83.34	0.28	81.35	0.56	81.04	0.56	21.62
89.35	0.47	87.21	0.70	86.74	0.70	21.89
95.70	0.62	93.40	0.82	92.77	0.82	22.17
102.38	0.74	99.91	0.94	99.12	0.94	22.45
109.40	0.87	106.76	1.07	105.82	1.07	22.74
116.79	1.01	113.97	1.21	112.87	1.21	23.04
124.55	1.13	121.53	1.33	120.29	1.33	23.34
132.69	1.25	129.46	1.46	128.07	1.46	23.66
141.25	1.40	137.80	1.62	136.26	1.62	23.98
150.25	1.64	146.57	1.85	144.89	1.85	24.32
159.76	1.98	155.83	2.18	154.01	2.18	24.66
169.91	2.46	165.72	2.64	163.75	2.65	25.01
180.82	3.01	176.35	3.19	174.24	3.19	25.37
192.56	3.55	187.79	3.72	185.54	3.72	25.74
205.15	4.05	200.06	4.22	197.67	4.22	26.12
218.58	4.53	213.15	4.70	210.61	4.70	26.52
232.81	5.01	227.01	5.19	224.34	5.20	26.93
247.87	5.54	241.68	5.73	238.87	5.73	27.35
263.84	6.11	257.25	6.30	254.29	6.30	27.78
280.86	6.72	273.83	6.92	270.72	6.92	28.22
299.09	7.32	291.58	7.53	288.34	7.53	28.69
318.61	7.96	310.61	8.18	307.21	8.18	29.16
339.56	8.71	331.01	8.94	327.47	8.94	29.66
362.01	9.64	352.88	9.89	349.18	9.89	30.16
386.21	10.78	376.45	11.03	372.59	11.03	30.69
412.29	12.07	401.85	12.32	397.81	12.33	31.24
440.27	13.39	429.09	13.66	424.88	13.67	31.80
470.42	14.91	458.44	15.18	454.04	15.19	32.39
503.01	16.39	490.17	16.68	485.59	16.68	33.00
538.20	17.92	524.42	18.23	519.64	18.23	33.63
576.09	19.48	561.30	19.81	556.32	19.81	34.29
616.85	21.24	600.97	21.59	595.77	21.60	34.97
660.76	23.26	643.70	23.64	638.27	23.64	35.68
708.13	25.65	689.78	26.06	684.12	26.06	36.42
759.43	28.57	739.67	29.00	733.77	29.00	37.20
815.09	32.02	793.80	32.46	787.65	32.46	38.00
875.66	35.86	852.71	36.33	846.29	36.33	38.84
941.52	39.88	916.75	40.38	910.05	40.38	39.72
1013.13	44.46	986.37	44.99	979.38	44.99	40.64
1092.66	50.00	1063.69	50.55	1056.39	50.55	41.60
1180.37	55.98	1148.96	56.57	1141.33	56.58	42.61
1277.07	62.79	1242.97	63.42	1234.99	63.42	43.67
1383.70	70.46	1346.61	71.13	1338.27	71.13	44.79
1501.41	79.06	1461.00	79.78	1452.26	79.79	45.96
1631.59	89.11	1587.49	89.88	1578.34	89.88	47.20
1776.75	101.83	1728.53	102.65	1718.93	102.65	48.50
1939.11	116.49	1886.26	117.37	1876.19	117.37	49.88
2123.13	139.45	2065.04	140.34	2054.46	140.35	51.34
2310.89	168.21	2247.49	169.11	2236.41	169.11	52.73

TABLE I. The Ta measured longitudinal stress, reduced isentrope and reduced isotherm in tabulated form.